ChemCatChem

Research Article
doi.org/10.1002/cctc.202500490

Chemistry Europe
European Chemical Societies Publishing

www.chemcatchem.org

# Graphene as a Suitable Support for Nickel Nanoparticles Functionalized with NHC Ligands in Dehydrogenation of Alcohols

Judith Medina-Vargas,[a] Andrés Mollar-Cuni,[a] Santiago Martín,[b, c] Iván Sorribes,*[a] and Jose A. Mata*[a]

In this paper, we describe a bottom-up synthesis of nickel nanoparticles (NiNPs) functionalized with *N*-heterocyclic carbene ligands and immobilized onto reduce graphene oxide (**rGO**). This tailored synthetic approach provides insights into the physical and chemical factors influencing NiNP formation and properties. The hybrid material (metal nanoparticles + organic ligand + graphene) is prepared starting from a well-defined nickel complex that is decomposed in a controlled manner providing ligand-decorated metal nanoparticles under mild conditions. The resulting NiNPs are spherical, with a small average size distribution (3.7 ± 0.9 nm). This hybrid material (**NiNPs/NHC@rGO**) is an efficient catalytic material for the dehydrogenation of alcohols to produce carbonyls with the concomitant release of molecular hydrogen. We explore its catalytic properties, substrate scope, and recyclability. Furthermore, X-ray photoelectron spectroscopy analysis reveals the material's evolution over multiple catalytic cycles. The reusability of NiNPs on graphene represents a significant advancement in the design of nickel-based catalytic materials.

## 1. Introduction

The development of sustainable catalytic transformations requires the use of catalytic materials that do not rely on critical metals.[1–4] In this context, nickel nanomaterials (NiNPs) have gained significant attention due to their proven efficiency in various catalytic systems,[5] including carbon–carbon[6–10] and carbon-heteroatom couplings,[11–13] hydrogenation,[14–16] hydrogen/deuterium exchange,[17,18] hydrosilylation,[19,20] and oxidation/reduction reactions including water splitting.[21–24] However, the number of applications is still limited compared to platinum group metals.[25] Enhancing the catalytic performance of first row transition metals requires tuning active sites through ligand design, the use of suitable additives (e.g., capping agents, surfactants) or supports.[26–28] Nickel-based materials are usually prepared by impregnation of a nickel salt, followed by thermal or chemical reduction to form metal nanoparticles (MNPs).[29–31] It is well-established that NiNPs exhibit distinct properties from their bulk counterparts, and more importantly, their reactivity can be modulated through appropriate additives and supports.[32] The rational design of nanomaterials enables control over catalytic performance, stability, and selectivity, which are critical for efficient transformations. Previously, we investigated the influence of graphene as a support for palladium nanoparticles (PdNPs).[33] Graphene provided stability by preventing sintering and Ostwald ripening during catalytic alkyne hydrogenation. We also explored how various ligands affect the catalytic properties of gold nanoparticles (AuNPs) immobilized onto the surface of graphene.[34] The ligands containing groups that favor stronger interactions with the support provided the most efficient catalytic materials. Other studies have also demonstrated the impact of stabilizers and supports on NiNP-based catalysis. For example, García et al. reported that NiNPs supported on defective graphene, thermally derived from sodium alginate, serve as efficient photocatalysts for $CO_2$ reduction in the gas phase, even in the absence of stabilizers or ligands.[21] Additionally, Godard et al. described NiNPs decorated with *N*-heterocyclic carbene ligands and immobilized on carbon nanotubes as effective catalyst in selective semihydrogenation of alkynes (Figure 1).[14]

Dehydrogenation of alcohols with the concurrent formation of molecular hydrogen is an interesting transformation from the academic point of view but also from the hydrogen storage technologies using C—H bonds, such as those based on liquid organic hydrogen carriers (LOHCs).[35–41] Traditionally, noble metal-based heterogeneous catalysts (e.g., Pd, Pt, and Ru) have

[a] J. Medina-Vargas, Dr. A. Mollar-Cuni, Dr. I. Sorribes, prof. Dr. J. A. Mata
Institute of Advanced Materials (INAM), Universitat Jaume I, Avda. Sos Baynat s/n, Castellón 12071, Spain
E-mail: isorribe@uji.es
jmata@uji.es

[b] Dr. S. Martín
Instituto de Nanociencia y Materiales de Aragón (INMA), CSIC-Universidad de Zaragoza, Zaragoza 50009, Spain

[c] Dr. S. Martín
Departamento de Química Física y Laboratorio de Microscopias Avanzadas (LMA), Universidad de Zaragoza, Edificio I+D+i., Zaragoza 50018, Spain

Supporting information for this article is available on the WWW under https://doi.org/10.1002/cctc.202500490

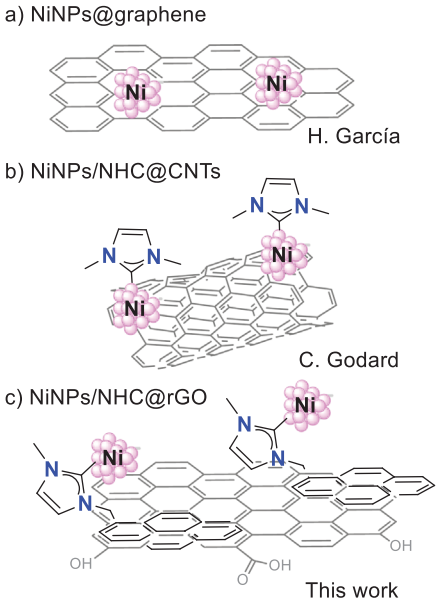


**Figure 1.** NiNPs based catalytic materials.

been employed for this purpose, but their scarcity and high cost pose significant challenges for large-scale industrial implementation. Given the global energy transition strategies and the increasing importance of green hydrogen, the development of catalytic systems based on abundant and cost-effective metals is highly desirable.[42–44]

In this study, we describe the catalytic properties of NiNPs functionalized with *N*-heterocyclic carbene ligands anchored onto **rGO** for the dehydrogenation of alcohols. The hybrid catalytic material is prepared using a modular approach starting from a well-defined nickel molecular complex. This strategy allows a rational and controlled procedure for the synthesis of NiNPs.

## 2. Results and Discussion

### 2.1. Synthesis and Characterization

Nickel nanoparticles decorated with *N*-heterocyclic carbene ligands (NHCs) and supported on reduced graphene oxide (**rGO**) were prepared in a sequential way to enable precise control over the final morphology and composition (Scheme 1). The first step in the synthetic procedure consists in the preparation of a well-defined nickel complex **2** (Figures S1–S9). The ligand precursor **1,** containing an NHC with Me- and methyl pyrene substituents, previously reported by our group, was metalated using nickelocene as metal precursor. The driving force of the reaction is the transformation of a 20-electron valence shell complex to a more stable 18-electron complex where one cyclopentadienyl group ($C_5H_5^-$) of nickelocene acts as an internal base for deprotonation of imidazolium salt (**1**) forming cyclopentadiene ($C_5H_6$).[25,45–47] The resulting cyclopentadienyl Ni complex **2** was characterized by NMR spectroscopy, electrospray ionization–mass spectrometry (ESI–MS), X-ray photoelectron spectroscopy (XPS), thermogravimetric analysis (TGA), and single crystal X-ray diffraction. The molecular structure of complex **2** confirms the expected half-sandwich structure with a bromo and a NHC ligand forming a dihedral angle of 94.2 (Figure 2a).

The immobilization of complex **2** onto **rGO** provided the hybrid material **2-rGO**, facilitated by $\pi$-stacking interactions between the pyrene tag and the graphene support. Although, these noncovalent interactions are relatively weak, their multiplicity in the case of graphene enhances stability, as we have previously observed with other metal complexes.[48–53] Indirect evidence of the tendency of metal complexes to engage $\pi$-staking interactions is observed in the packing diagram of complex **2** (Figure 2b). The crystal packing reveals pairs of molecules in proximity, displaying $\pi$-stacking interactions between the pyrene tags with an interplanar distance of 3.52 Å. The grafting procedure was carried out by stirring the **rGO** support in a $CH_2Cl_2$ solution of complex **2** at room temperature. The use of mild conditions ensured the preservation of the material's properties and morphology. Characterization of the hybrid material **2-rGO** by HRTEM confirmed the homogeneous distribution of complex **2** over the 2D surface of graphene (Figures S10 and S11).

The hybrid material **2-rGO** was used to synthesize **NiNPs/NHC@rGO** through two methods. Method A involves a controlled reduction of metal complex **2** using borane t-butylamine ($^tBuNH_2$-$BH_3$) as reducing agent. Alternatively, in method B, **NiNPs/NHC@rGO** can be synthesized directly from complex **2** in the presence of a **rGO** suspension, using the same reducing agent. Both methods result in nickel nanoparticles that are directly immobilized onto the surface of graphene, exhibiting the same morphology (comparison in Figures S12 and S13). The final hybrid material, **NiNPs/NHC@rGO**, appears as a fine black powder, which remains stable for months in the solid state.

Characterization of **NiNPs/NHC@rGO** was performed using different microscopic, spectroscopic, and analytical techniques. Detailed procedures and additional data are provided in the Supporting Information. HRTEM microscopy confirms the 2D morphology of **rGO** and the homogeneous distribution of nickel on its surface (Figure 3 and Figures S12–S15). The low contrast of nickel transmission microscopy due to small particle size and low atomic number, impedes a clear visualization of metal nanoparticles in regions where the graphene layers overlapped. However, well-defined spherical metal nanoparticles are observed at the edges (Figure 3). The size histogram analysis provides an average diameter of 3.7 $\pm$ 0.9 nm (Figure 3c). We performed a comparative analysis of **rGO** and **NiNPs/NHC@rGO** by X-ray diffraction (XRD) to determine sample's composition and crystallinity. However, no significant differences were observed in the diffraction pattern due to the intrinsic lamellar structure of **rGO** and the low ratio of **NiNPs** versus support (Figure S16). The characteristic diffraction peaks corresponding to metallic nickel (JCPDS card no. 04-0850) were not detected, with the only intense diffraction peaks attributed to **rGO**.[54,55] The presence of defects in the support was assessed using Raman spectroscopy. The introduction of nickel nanoparticles onto the surface of **rGO** had minimal impact on the relative intensity of the graphitic ($I_G$ at

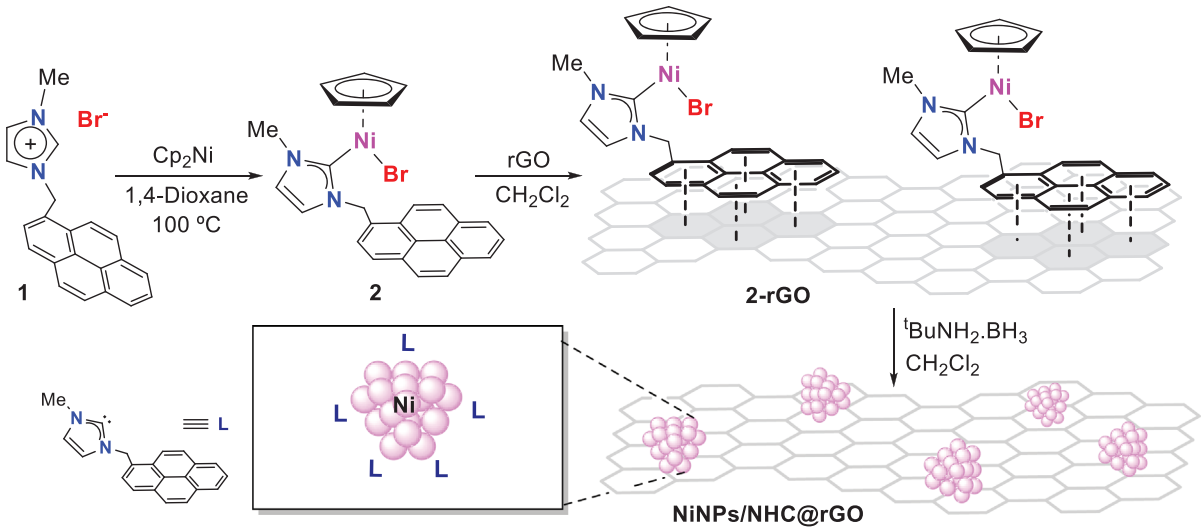


**Scheme 1.** Synthesis of nickel nanoparticles functionalized with NHC ligands supported onto **rGO**.

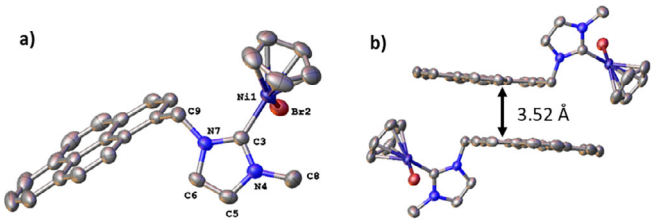


**Figure 2.** Single crystal X-ray diffraction. a) Molecular structure of complex **2** and b) packing diagram showing the interplanar distance between the pyrene tags of 3.52 Å.

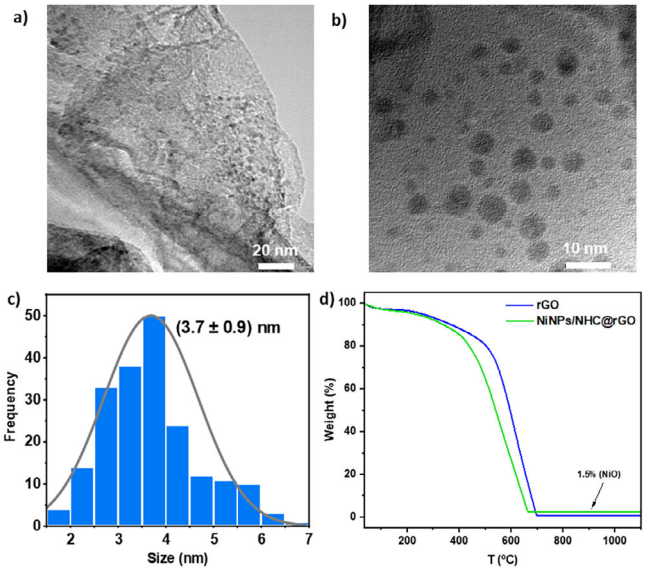


**Figure 3.** Characterization of **NiNPs/NHC@rGO**. a) HRTEM image, b) STEM image, c) size histogram ($N = 200$), and d) comparative thermogravimetric analysis of **rGO** with/without nickel nanoparticles.

1590 $cm^{-1}$) and defect ($I_D$ at 1350 $cm^{-1}$) bands, when comparing the Raman spectra of **rGO** and **NiNPs/NHC@rGO** (Figure S17).[56] This suggests that the formation and immobilization of metal nanoparticles does not affect the graphene character of **rGO**, most probably due to the low **NiNPs**-to-support ratio. FTIR spectroscopy provided the characteristic fingerprint of each material with subtle differences observed for the graphene containing NiNPs sample (Figure S18). Then, we performed the characterization of the material by TGA. We started our studies by analyzing the thermal decomposition of complex **2**. The thermogram of **2** provided characteristic mass losses corresponding to different ligands fragments (Figures S19 and S20). Up to 400 °C, a 26.5% mass loss was observed, attributed to the elimination of Cp and Br. Between, 400–600 °C, and additional 58.1% mass loss was recorded, corresponding to the decomposition of the NHC ligand, confirming its thermal stability. Beyond 600 °C, the remaining 15.4 wt% was identified as nickel in the form of nickel oxide (NiO).

A comparative TGA of **rGO** and **NiNPs/NHC@rGO** was then performed under both nitrogen and air atmospheres, with the most informative results obtained in air. The thermogram for both materials under air shows a sharp mass loss between 400 and 600 °C (Figure 3d). Notably, the residual mass observed for **NiNPs/NHC@rGO** was 1.5 wt% that corresponds to the total amount of nickel content in the material assuming complete oxidation to NiO. The nickel content in **NiNPs/NHC@rGO** was further quantified using ICP-MS. The sample was digested using a mixture of $HNO_3$/HCl acids under microwave irradiation (45 min) to ensure complete nickel solubilization. The nickel content on **NiNPs/NHC@rGO** was 1.14 wt% indicating that almost all initial nickel was anchored onto the support (Figure 3d). The nickel content obtained from ICP-MS closely matched the results from TGA, considering the formation of NiO.

We performed a comprehensive characterization analysis using XPS by comparison of the spectra of complex **2** and the material **NiNPs/NHC@rGO** (Figure 4). The survey spectrum and further details of XPS analysis are provided in the supporting information (Figures S21 and S22). The XPS analysis of complex **2** is straightforward, as its elemental composition and nickel oxidation state is predetermined and well established by other techniques. The survey spectrum is primarily characterized by signals corresponding to carbon, nickel, nitrogen,

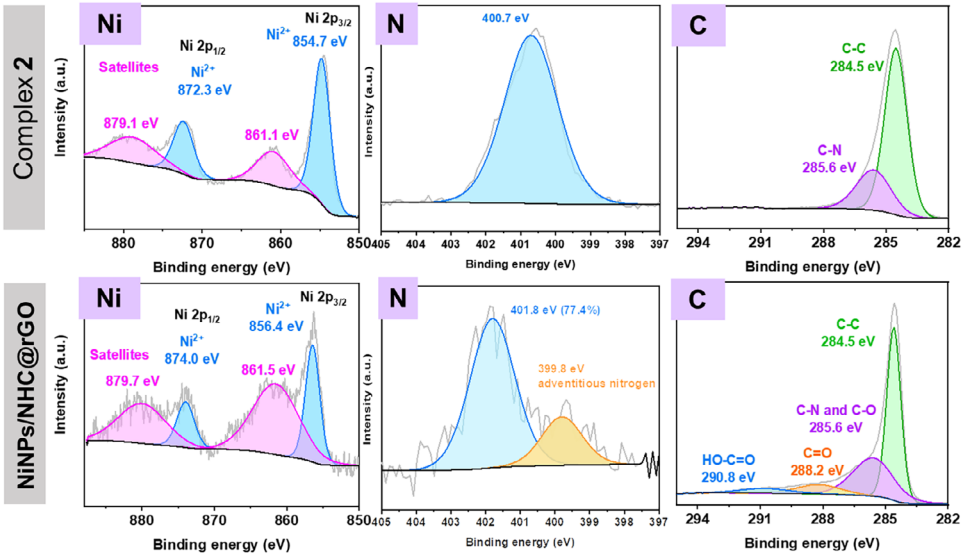


**Figure 4.** Comparative XPS analysis of complex **2** and **NiNPs/NHC@rGO** corresponding to the high-resolution core-level peaks of Ni(2p), N(1s), and C(1s).

bromo, and adventitious oxygen. The high-resolution core-level peak of Ni2p in complex **2** exhibits two distinct peaks corresponding to Ni $2p_{1/2}$ (872.3 eV) and Ni $2p_{3/2}$ (854.7 eV), along with their corresponding satellite peaks at 879.1 and 861.1 eV, respectively. These peaks are unequivocally assigned to the $Ni^{2+}$ oxidation state. Another key feature is the high-resolution peak of C 1s that is dominated by C—C(H) groups (284.5 eV) from the NHC and Cp ligands. The asymmetry of C 1s peak at higher binding energies suggests the presence of C—N groups (285.6 eV) which are associated with the azole ring. This assignment is further supported by the N 1s spectrum, where a peak at 400.7 eV corresponds to nitrogen within the azole ring.

The survey spectrum of **NiNPs/NHC@rGO** is primarily composed of signals from carbon, nickel, nitrogen, and oxygen, with no detectable bromine, indicating its lost during the formation of nickel nanoparticles. The high-resolution core-level peak of Ni 2p closely resembles that of the molecular complex; however, the core-level peaks are shifted to higher binding energies, which is attributed to nanoparticle formation. Specifically, the core level peak of Ni $2p_{1/2}$ shifts from 872.3 to 874.0 eV, while the peak of Ni $2p_{3/2}$ from 854.7 to 856.4 eV.[21] These peaks positions correspond to nickel in the +2 oxidation state, likely in the form of NiO, as further supported by the **O 1s** spectrum, which exhibits a characteristic peak at **530.3 eV** (Figure S22). The Ni 2p spectrum did not reveal any contribution of $Ni^0$ oxidation states of metallic nickel particles most probably due to the presence of NHC ligands covering the surface of the nanoparticle as it is corroborated by the displacement at higher binding energies observed in the N 1s region for the peak attributed to the azole ring (from 400.7 to 401.8 eV).[57] We and others have previously observed the absence of low valence metal species in AuNPs covered with NHC ligands by XPS. Most probably due to the low penetration of XPS radiation especially when bulky NHC ligands are used.[58,34] Using XPS we cannot exclude the presence of Ni(0) species in the core of NiNPs. The high-resolution peak of C 1s in **NiNPs/NHC@rGO** is dominated by C—C(H) groups (284.5 eV) but deconvolution of the peak confirmed the presence of C—O single (290.8 eV) and C═O double bond (288.2 eV) groups characteristic of graphene materials.

### 2.2. Catalytic Properties in the Conversion of Benzyl Alcohols

We assessed the catalytic properties of the hybrid material **NiNPs/NHC@rGO** in the conversion of benzylic alcohols into aldehydes with the concomitant formation of $H_2$. We used benzylalcohol as model substrate for the optimization of the catalytic reaction conditions (Table 1). Control experiments confirmed the necessity of both the catalyst and base, as no alcohol conversion was observed in their absence. To further assess the catalytic role of the support, we tested **rGO** alone as a carbocatalyst (Table 1, entry 1). However, **rGO** did not promote efficient dehydrogenation of alcohols into aldehydes, despite its known catalytic activity in the oxidation of alcohols using molecular oxygen as the oxidant.[59–67] The properties of **rGO** as carbocatalyst have recently been disclosed in dehydrogenation of *N*-heterocycles but, to the best of our knowledge, its application in alcohol dehydrogenation has not yet been demonstrated.[68,69] Control experiments confirmed nickel nanoparticles (NiNPs) as the catalytic active sites for converting primary alcohols into aldehydes. While the support itself lacks catalytic activity in this transformation, it plays a main role in the stability of metal nanoparticles and influences their formation. This aligns with our prior observations of the noninnocent role of the support in the case of metal complexes[50,53,70,71] and metal nanoparticles[56,72] anchored on the surface of **rGO**. We assessed a variety of solvents for dehydrogenation of alcohols using **NiNPs/NHC@rGO** (Table 1, entries 2–8). The reaction proceeded with different solvents providing better results using solvents containing an aromatic group. Among all, the best results were obtained with toluene. When doing the reaction at lower substrate concen-

**Table 1.** Reaction optimization using benzyl alcohol as model substrate.

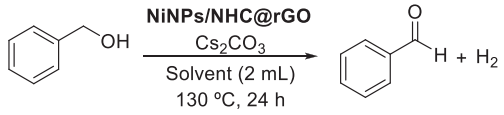


| Entry | Solvent | Temp. (°C) | Base (mmol) | Conv. (%)[a] | Yield (%)[a] | TON[b] | TOF ($h^{-1}$)[b] |
|---|---|---|---|---|---|---|---|
| 1[c] | Toluene | 130 | 0.30 | 0 | 0 | 0 | 0 |
| 2 | Chlorobenzene | 130 | 0.30 | 96 | 75 | 44 | 1.8 |
| 3 | Toluene | 130 | 0.30 | 100 | 94 | 55 | 2.2 |
| 4 | THF | 130 | 0.30 | 6 | 3 | 1.8 | 0.1 |
| 5 | MeCN | 130 | 0.30 | 29 | 2 | 1.2 | 0.1 |
| 6 | *p*-Xylene | 130 | 0.30 | 80 | 61 | 36 | 1.5 |
| 7 | *o*-Xylene | 130 | 0.30 | 44 | 39 | 23 | 1 |
| 8 | *n*-hexane | 130 | 0.30 | 63 | 60 | 35 | 1.5 |
| 9 | Toluene (3 mL) | 130 | 0.30 | 77 | 76 | 45 | 1.9 |
| 10 | Toluene | 130 | 0.15 | 76 | 52 | 31 | 1.3 |
| 11 | Toluene | 130 | 0.45 | 95 | 81 | 48 | 2 |
| 12 | Toluene | 130 | 0.3 (NaOH) | 64 | 36 | 21 | 0.9 |
| 13 | Toluene | 100 | 0.30 | 29 | 19 | 11 | 0.5 |
| 14[d] | Toluene | 130 | 0.30 | 59 | 52 | 10 | 0.4 |
| 15[e] | Toluene | 130 | 0.30 | 74 | 72 | 14 | 0.6 |
| 16[f] | Toluene | 130 | 0.30 | 53 | 52 | 10 | 0.4 |

**General reaction conditions**: benzyl alcohol (0.15 mmol), catalyst loading (1.7 mol% Ni based on surface atoms), base (0.3 mmol), 130 °C, and solvent (2 mL).
[a] Conversion and yield determined by gas chromatography using anisole (0.15 mmol) as an internal standard.
[b] TON and TOF values at 24 h.
[c] Using **rGO** (15 mg), without nickel, as a carbo-catalyst.
[d] Using NiNPs onto **rGO** without NHC ligand.
[e] Using **2-rGO** as catalyst (5 mol% based on Ni).
[f] Using the molecular complex **2** as catalyst (5 mol% based on Ni).

tration (0.05 M) the results were diminished (Table 1, entry 9). Variation in the amount of base or substituting cesium carbonate by NaOH did not have any improvement in the reaction (Table 1, entries 10–12). We also evaluated the role of the NHC ligand in dehydrogenation of alcohols. For that purpose, we prepared nickel nanoparticles anchored on **rGO** following the same procedure but using $NiCl_2$ as precursor instead of metal complex **2**. Using this material, we observed a lower conversion/yield in dehydrogenation of benzylalcohol (Table 1, entry 14). It is important to note that the molecular complex **2** or the catalytic material containing this complex immobilized through $\pi$-stacking interactions are also active in this transformation although lower activity was observed, likely due to decomposition of **2** (Table 1, entries 15 and 16). These findings underscore the NHC ligand's critical function in modulating the catalytic properties of nickel nanoparticles. Optimization of reaction conditions confirmed that the best results were obtained using **NiNPs/NHC@rGO** under the specific conditions described in entry 3 (Table 1).

The catalytic properties of **NiNPs/NHC@rGO** were evaluated by monitoring the reaction evolution using GC-FID. Reaction profiles provide valuable information about catalytic procedures and are particularly convenient to detect catalyst deactivation and/or the presence of induction periods. We monitored the reaction evolution using benzylalcohol as model substrate under the general conditions previously described (Figure 5). The reaction profile corresponds to the characteristic logarithmic curves

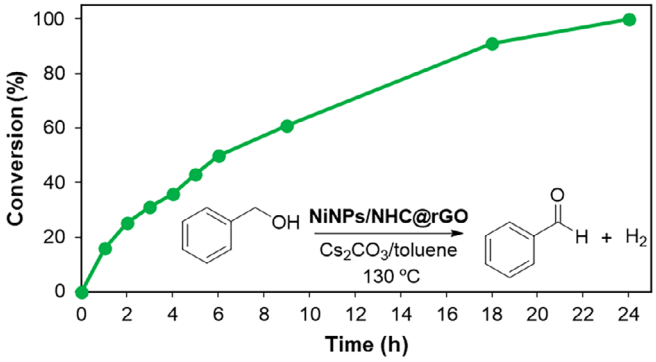


**Figure 5.** Reaction monitoring in the dehydrogenation of benzyl alcohol. Conditions: benzyl alcohol (0.15 mmol), catalyst loading (1.7 mol% Ni based on surface atoms or 5 mol% based on the total amount of Ni obtained by ICP-MS), base (0.3 mmol), 130 °C, and solvent (2 mL). Metrics at 1 h (TON = 9.4 and TOF = 9.4 $h^{-1}$), at 50% conversion (TON = 29.4 and TOF = 4.8 $h^{-1}$) and at the end of the reaction (TON = 58.8 and TOF = 2.5 $h^{-1}$).

without observing catalyst deactivation. We have not observed the presence of an induction period under our reaction conditions. Catalyst loading is a key parameter to establish the performance metrics of a catalytic system. In our case, we used a catalyst loading of 5 mol% based on the total amount of Ni obtained by ICP-MS. However, not all nickel atoms are located at the nanoparticle surface acting as active sites. Considering that NiNPs are spherical with an average size of 3.7 ± 0.9 nm (Figure 3), we estimated the number of nickel atoms located at the surface of the nanoparticles (Table S2 and Figure S23). This translates to only 34.5% of the total nickel atoms as accessible sites, indicating that the effective catalyst loading is 1.7 mol%. This value is the surface-specific activity defined for heterogeneous catalysts. The catalyst loading is significantly lower than conventional nickel-catalyzed systems (5–10 mol%) yet demonstrating comparable efficiency.

We evaluated the catalyst performance under different conditions relevant to elucidate its heterogeneous nature. When using solid catalysts, diffusion problems are often an important issue to consider for understanding the kinetics of the process. We assessed the influence of diffusion by monitoring the dehydrogenation of benzylalcohol at different stirring speeds (Figure 6a). The results in dehydrogenation of benzylalcohol at different revolutions per minute (100, 300, and 800) shows that the three plots overlapped suggesting that diffusion issues are negligible for this transformation. Most probably, the use of the 2D support with a high specific surface area allows the interaction of catalyst active sites with reagents. We then evaluated the influence of catalyst loading in dehydrogenation of alcohols (Figure 6b). The reaction profiles revealed a clear dependence of catalytic performance on the amount of catalyst used, demonstrating that higher catalyst loading enhances reaction efficiency.

Next, we assessed the reaction scope in dehydrogenation of alcohols using substrates with different functional groups. The progress of the reaction was evaluated independently by substrate disappearance (conversion) and product formation (yield). Conversion was obtained by GC/FID using anisole as an internal standard and yield was calculated by $^{1}$H NMR spectra using 1,3,5-trimethoxybenzene as an external standard (Table 2). The catalytic material **NiNPs/NHC@rGO** is active in the conversion of a series of benzyl alcohols into the corresponding aldehydes in good to excellent yields regardless of having electron-donating or electron-attracting groups. $^{1}$H NMR spectra of crude reaction mixture confirmed high selectivity, in alcohol dehydrogenation induced by **NiNPs/NHC@rGO,** showing only the aldehyde product and unreacted starting material without side products (Figures S24–S34). Substrates with *p*-substituted alkyl groups, such as *p*-methylbenzyl alcohol (Table 2, entry 1), *p*-isopropyl alcohol (Table 2, entry 3), *p*-$^{t}$butylbenzyl alcohol (Table 2, entry 5), and *p*-methoxybenzyl alcohol (Table 2, entry 2), were efficiently converted into the corresponding aldehydes, such as it is also the case of 2-naphthalenemethanol (Table 2, entry 6). Interesting results were also obtained in the case of piperonyl alcohol providing piperonal in 92% yield, a substance used in the synthesis of some pharmaceutical drugs such as L-DOPA, tadalafil, or atrasentan (Table 2, entry 4). Evaluation of the effect

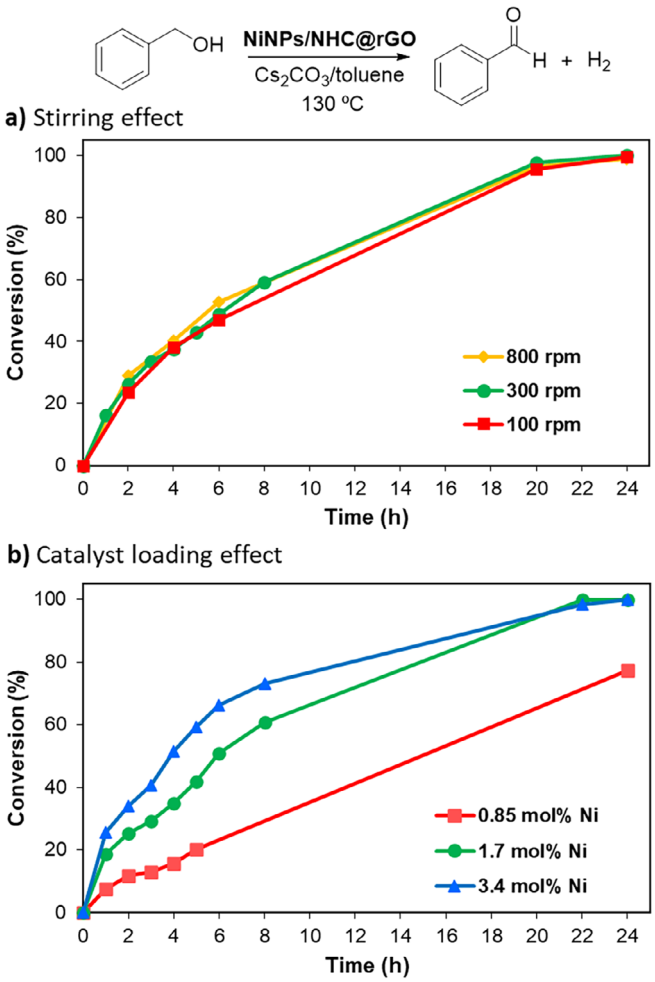


**Figure 6.** Reaction kinetics in the dehydrogenation of benzyl alcohol. a) Stirring effect and b) catalyst loading effect. Conditions: benzyl alcohol (0.15 mmol), catalyst loading (in mol% based on surface Ni atoms), base (0.3 mmol), 130 °C, and solvent (2 mL).

of halide (Cl) substitution at different positions (*ortho*, *meta*, and *para*) resulted in almost quantitative conversions except in the case of the ortho substituted substrate, which was converted to a lesser extent (72%) likely due to steric hindrance (Table 2, entries 7–9). In the case of bromide derivatives, a similar tendency was observed (Table 2, entries 10 and 11). However, in the case of iodide substituent, partial dehalogenation was observed (Table 2, entry 12) along with dehydrogenation. Benzyl alcohol with and without *o*-iodide substitution was observed as determined by GC-FID. This behavior may be attributed to the lability of iodide group. The reaction scope properties suggest that nickel nanoparticles functionalized with *N*-heterocyclic carbene ligands **NiNPs/NHC@rGO** is an efficient catalytic material in dehydrogenation of benzyl alcohols.

### 2.3. Recycling and Reusability Experiments

The stability of **NiNPs/NHC@rGO** was evaluated through recycling experiments assessing its performance in dehydrogenation of alcohols using identical reactions conditions across consec-

**Table 2.** Reaction scope in alcohol dehydrogenation.

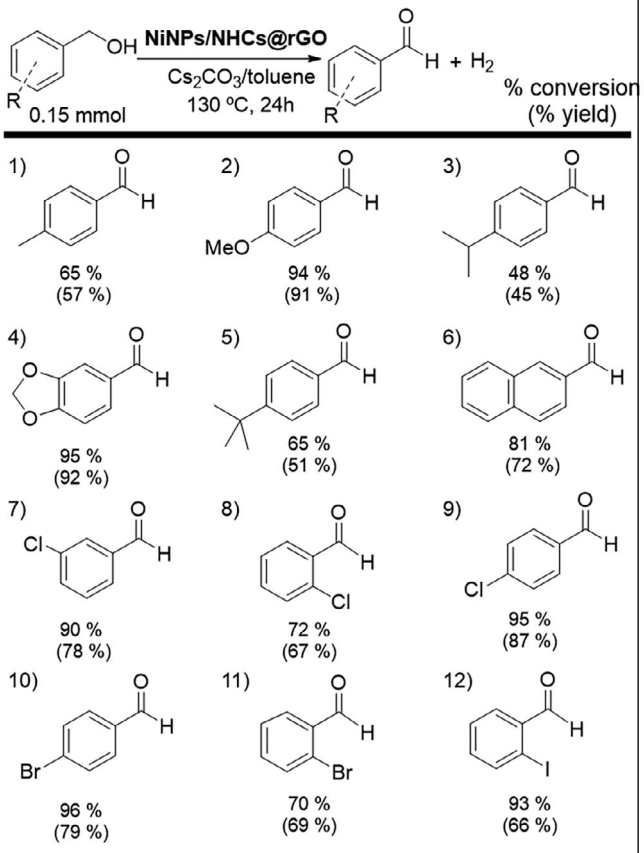


| Entry | 1 | 2 | 3 | 4 | 5 | 6 | 7 | 8 | 9 | 10 | 11 | 12 |
|---|---|---|---|---|---|---|---|---|---|---|---|---|
| $TON_{24h}$ | 34 | 54 | 26 | 54 | 30 | 42 | 46 | 39 | 51 | 46 | 41 | 39 |
| $TOF_{24h}$ ($h^{-1}$) | 1.4 | 2.3 | 1.1 | 2.3 | 1.3 | 1.8 | 1.9 | 1.6 | 2.1 | 1.9 | 1.7 | 1.6 |

*Note:* Reaction conditions: benzyl alcohol (0.15 mmol), catalyst loading (1.7 mol% Ni based on surface atoms), base (0.3 mmol), 130 °C, solvent (2 mL). Conversion calculated by GC/FID using anisole as an internal standard. Yield calculated by $^1$H NMR using 1,3,5-trimethoxybenze as an external standard.

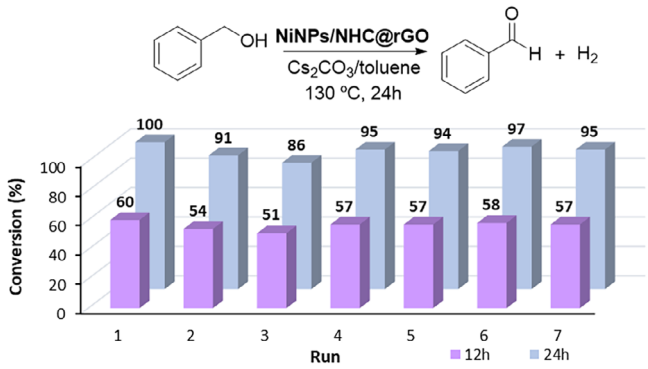


**Figure 7.** Recycling properties of **NiNPs/NHC@rGO**.

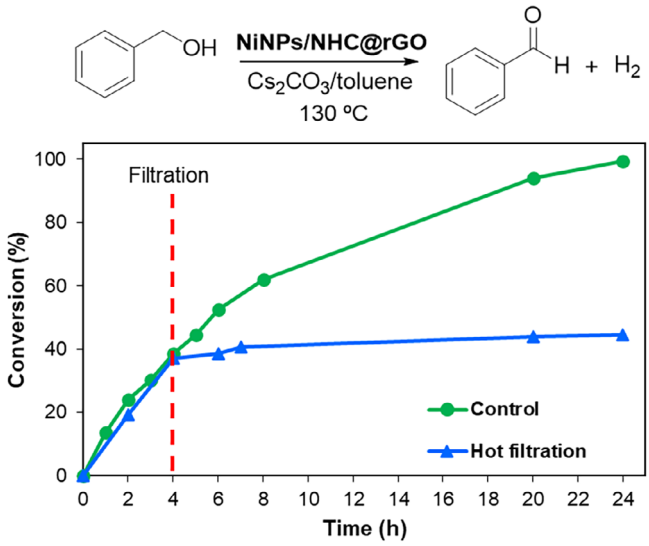


**Figure 8.** Hot filtration experiment. Initial conditions: benzyl alcohol (0.15 mmol), catalyst loading (1.7 mol% Ni based on surface atoms), $Cs_2CO_3$ (0.3 mmol), 130 °C, and solvent (2 mL). After filtration, $Cs_2CO_3$ (0.15 mmol) was added to the filtrate.

utive runs (Figure 7). The catalytic material was analyzed by spectroscopic and spectrometric techniques after a selected number of cycles to establish any change in the support or catalytic active species. The recycling properties were examined using benzyl alcohol as a model substrate under the standard conditions established for the reaction scope. In each cycle, the catalytic activity of **NiNPs/NHC@rGO** was analyzed twice (after 12 h and again at 24 h reaction) to prevent artifacts resulting from excess catalyst. When the reaction was finished, the solid catalyst was recovered by filtration and was thoroughly washed with toluene (3 × 5 mL), water (3 ×5 mL), and acetone (2 × 5 mL). Once the solid material was air-dried, it was reused in another catalytic cycle, under the same reaction conditions, without requiring reactivation. The results demonstrated that **NiNPs/NHC@rGO** maintained its catalytic performance for at least seven consecutive runs without noticeable deactivation. The catalyst's activity remained consistent after 12 h or at the end of the reaction (24 h), indicating that no deactivation is occurring over time. The stability of **NiNPs/NHC@rGO** was further assessed by hot filtration experiments to discard deactivation caused by leaching of active species as a common process in supported catalysis. The results of hot filtration experiments showed that after filtration of the solid catalyst the reaction ceased to progress (Figure 8). The absence of nickel species in the filtrate was further confirmed by ICP/MS analysis. These experiments confirm that the catalytic dehydrogenation of alcohols is heterogeneous in nature and occurs at the surface of graphene.

After completing the reusability experiments, we characterized the spent material (after the seventh run) to assess any potential structural changes. To this end, the reused hybrid material was analyzed using XPS spectroscopy (Figure 9 and Figures S35–S37). We compared the high-resolution peaks of main elements (Ni, O, N, and C) in the as-prepared **NiNPs/NHC@rGO** with the same material after one and seven catalytic runs. XPS analysis of high-resolution $Ni2p_{3/2}$ peak confirmed that after seven runs, binding energies and ratios remained unchanged, indicating that the nature of the catalytic material **NiNPs/NHC@rGO** is preserved. Simi-

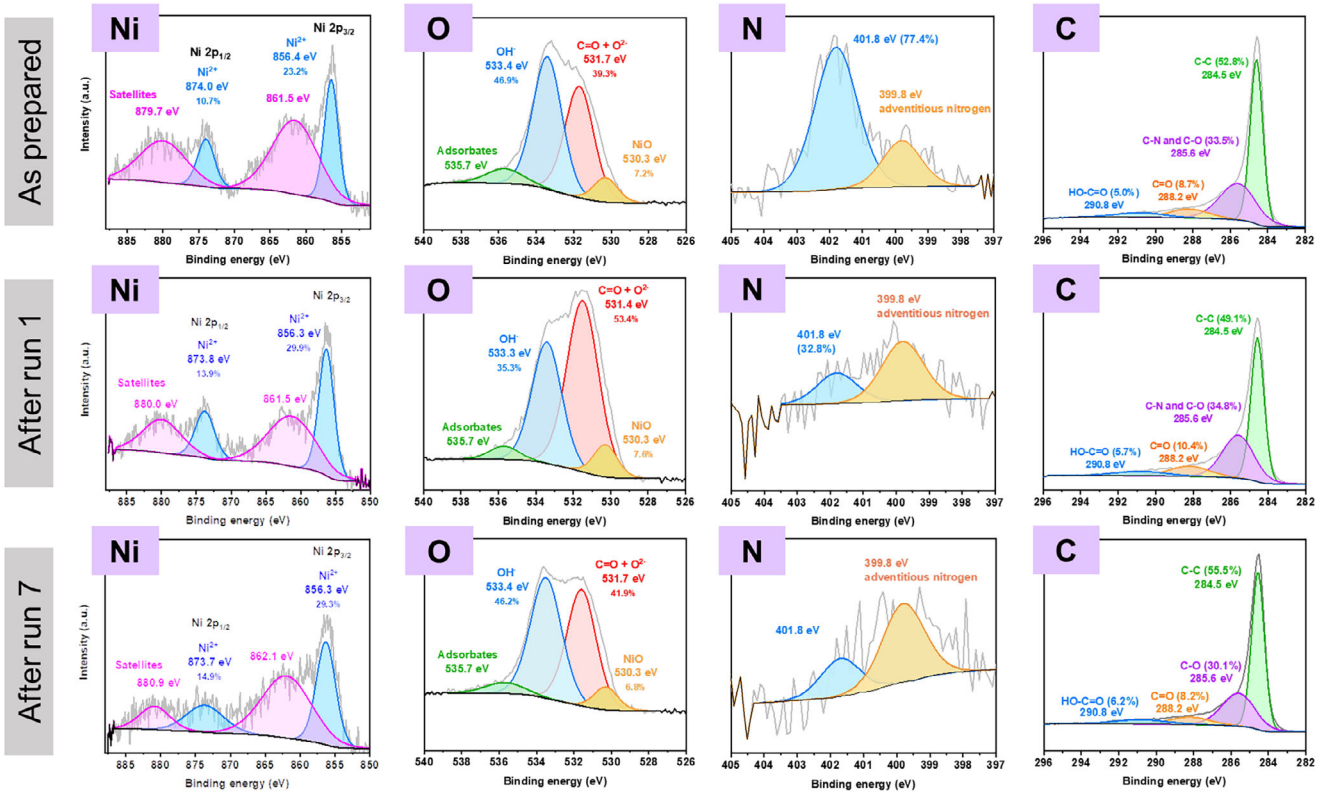


**Figure 9.** Comparative XPS characterization of **NiNPs/NHC@rGO** during recycling experiments. XPS analysis for the core-level peak of Ni2p, O1s, N1s, and C1s. Peaks of $Ni^{(2+)}$ in blue and satellites in pink.

larly, the high-resolution XPS spectra for N, O, and C showed no significant deviations, further confirming the stability of **NiNPs/NHC@rGO** after multiple reuses. These results suggest that the material **NiNPs/NHC@rGO** can be reused and recycled for at least seven runs without significant modifications of its structure.

## 3. Conclusions

There is a considerable interest in nickel materials with catalytic properties for replacing critical and scarce metals to develop more sustainable transformations. In this work, we have developed a hybrid material consisting of NiNPs decorated with NHC ligands and anchored onto the surface of reduce graphene oxide **(NiNPs/NHC@rGO)**. The heterogeneous catalyst effectively facilitates the dehydrogenation of alcohols to carbonyl compounds. The combination of the support and ligands enhances the stability of NiNPs, allowing the catalyst to be reused for at least seven cycles without noticeable deactivation. The improved catalytic performance of **NiNPs/NHC@rGO** constitutes a clear example of sustainable design of nickel-based catalytic materials.

## 4. Experimental Section

### 4.1. Materials and Methods

Reagents were obtained from commercial sources and were used as received. Solvents were dried using a solvent purification system. The ligand precursor bromomethyl pyrene was prepared according to reported procedures. **rGO** was purchased (Graphenea) and used as received.[73]

Nuclear magnetic resonance (NMR) spectra were recorded using Bruker spectrometers operating at 400.17 MHz ($^1$H NMR) and 100.63 MHz ($^{13}C\{^1H\}$ NMR), respectively, and referenced to $SiMe_4$ ($\delta$ in ppm and J in Hertz). NMR spectra were recorded at room temperature with the appropriate deuterated solvent.

High-resolution mass spectra (HRMS) were obtained using a QTOF Premier (quadrupole-hexapole-TOF) with an orthogonal Z-spray-electrospray interface (Waters, Manchester, UK).

High-resolution images of transmission electron microscopy (HRTEM) and high-angle annular dark-field images (HAADF-STEM) of the samples were obtained using a Jem-2100 LaB6 (JEOL) transmission electron microscope coupled with an INCA Energy TEM 200 (Oxford) energy dispersive X-ray spectrometer (EDX) operating at 200 kV. To prepare the samples, a droplet of methanol dispersion was dried on a carbon-coated copper grid.

The nickel content in the hybrid material was determined by inductively coupled mass spectrometry analysis (ICP-MS). The digestion of 15 mg sample material was performed in a Mars 6 iWave CEM microwave oven using nitric acid (69%) with a power of 1800 W at 210 °C for 45 min. After removal of solid particles by filtration and dilution to an appropriate volume, ICP-MS analysis was recorded on an Agilent 7500 CX instrument in duplicate.

TGA was performed using a TG-STDA Mettler Toledo model TGA/SDTA851e/LF/1600 coupled to a mass spectrometer quadrupole PFEIFFER VACUUM model OmniStar GSD 320 O3, 1–300 uma bearing a tungsten filament. The analysis was carried out heating 15 mg of sample in alumina pan from 35 to 1100 °C at 10 °C $min^{-1}$ using an air flow.

X-ray photoelectron spectra (XPS) were acquired on a Kratos AXIS ultra DLD spectrometer with a monochromatic Al K$\alpha$ X-ray source (1486.6 eV) using a pass energy of 20 eV. To provide a precise energy calibration, the XPS binding energies were referenced to the C 1s peak at 284.6 eV.

Raman spectra were recorded at room temperature using a 532 nm laser excitation focused through a WITec GmbH Raman spectrophotometer equipped with a CCD detector.

FTIR spectra were recorded at room temperature employing a Jasco FT/IR-6200 spectrophotometer with a *Jasco ATR Pro One dispositive*.

Gas chromatography (GC) analysis was obtained on a shimadzu GC-2010 apparatus equipped with FID detector and using a Teknokroma column (TRB-5MS; 30 m x 0.25 mm x 0,25 µm). Temperature program: 1) 80 °C, 10 °C $min^{-1}$ until 150 °C, 1 min. 2) 150 °C, 20 °C $min^{-1}$ until 300 °C, 2 min. Total time: 17.5 min.

### 4.2. Synthesis

***Synthesis of complex 2***: The imidazolium salt **1** (300 mg, 0.79 mmol), bis(cyclopentadienyl)nickel(II) (150 mg, 0.79 mmol), and dry 1,4-dioxane (12 mL) were mixed in a Schlenk tube under nitrogen atmosphere. The mixture was stirred at 100 °C for 17 h. Then, the reaction mixture was filtered through celite using a cannula transfer process, and the filtrate was concentrated under reduced pressure. The resulting red solid was redissolved in the minimum amount of $CH_2Cl_2$, precipitated with pentane, and isolated by filtration. Yield: 205 mg (52%). $^1$H NMR (400.17 MHz, $CDCl_3$) $\delta$ 8.45 (d, $^3J_{H,H}$ = 9.3 Hz, 1H, C*H*$_{pyr}$), 8.25–8.03 (m, 7H, C*H*$_{pyr}$), 7.79 (d, $^3J_{H,H}$ = 7.9 Hz, 1H, C*H*$_{pyr}$), 6.87 (d, $^3J_{H,H}$ = 1.7 Hz, 1H, C*H*$_{imid}$), 6.82 (d, $^3J_{H,H}$ = 13.4 Hz, 1H, NC*H*$_a$H$_b$—), 6.66 (d, $^3J_{H,H}$ = 13.4 Hz, 1H, NCH$_a$*H*$_b$—), 6.59 (d, $^3J_{H,H}$ = 1.7 Hz, 1H, CH$_{imid}$), 5.30 (s, 5H, C*H*$_{cp}$), 4.38 (s, 3H, NC*H*$_3$). $^{13}$C{$^1$H} NMR (100.63 MHz, $CDCl_3$) $\delta$ 162.7 (*C*$_{carbene}$–Ni), [131.7, 131.3, 130.8, 129.3, 128.9, 128.7, 128.0, 127.3, 127.0, 126.3, 125.7, 125.5, 125.1, 124.8, 124.6, 123.6, 122.9, 122.2] (CH$_{pyr}$, *C*H$_{imid}$), 91.8 (CH$_{cp}$), 54.2 (NCH$_2$—), 39.3 (NCH$_3$). HRMS ESI-TOF-MS (positive mode): m/z (fragment) 419.1062 $[M–Br]^+$; theoretical 419.1058.

***Synthesis of NiNPs/NHCs@rGO***: Method A: A suspension of 90 mg of **rGO** in 20 mL of $CH_2Cl_2$ was sonicated for 30 min. Complex **2** (10 mg) was then added, and the mixture was sonicated for an additional 5 min. The resulting mixture was stirred overnight at room temperature. Then, the solid was filtered off and washed with $CH_2Cl_2$ affording the hybrid material **2-rGO**. Next, the formation of NiNPs was accomplished by adding $^t$BuNH$_2$-BH$_3$ (1 mmol) as a reducing agent to a suspension of 50 mg of **2-rGO** in 20 mL of $CH_2Cl_2$. The mixture was stirred at room temperature for 16 h. Then, the solid was filtered, washed with $CH_2Cl_2$, and dried using acetone. Method B: A suspension of **rGO** (90 mg) in a solution of complex **2** (10 mg) in $CH_2Cl_2$ (20 mL) was sonicated for 30 min. Subsequently $^t$BuNH$_2$-BH$_3$ (2 mmol) was added slowly, and the mixture was stirred at room temperature for 16 h. After this time, the black solid formed was recovered by filtration, washed with $CH_2Cl_2$, MeOH, water, and ether; and then evaporated to dryness under reduced pressure. The total nickel amount in the material was quantified by ICP-MS, giving an experimental Ni content of 1.14 wt%.

### 4.3. Catalytic Procedures and Experiments

***Catalytic experiments***: In a general catalytic experiment, 0.15 mmol of alcohol, 2 equiv. of $Cs_2CO_3$, 1.7 mol% of Ni (considering the atoms of nickel on the surface of nanoparticles), and 2 mL of toluene were introduced in a round-bottom flask. Estimation of surface atoms in NiNPs was obtained considering a spherical morphology as described in section 10 of the Supporting Information. The flask was then introduced in a preheated 130 °C oil-bath for 24 h. Reaction evolution was performed by GC/FID taking aliquots at selected times and using anisole as an internal reference. Reaction yield was determined by $^1$H NMR using 1,3,5-trimethoxybenzene (TMB) as an external reference.

***Diffusion effects***: To a round-bottom flask, 0.15 mmol of benzyl alcohol, 2 equiv. of $Cs_2CO_3$, 1.7 mol% of Ni (surface atoms), and 2 mL of toluene were added. The flask was then introduced in a preheated 130 °C oil-bath and stirred at 100, 300, or 800 rpm for 24 h to evaluate diffusion limitations during the reaction. No significant differences were observed (Figure 6a), indicating that the kinetics or the reaction are not controlled by diffusion.

***Catalyst loading***: To a round-bottom flask, 0.15 mmol of benzyl alcohol, 2 equiv. of $Cs_2CO_3$, catalyst loading: 0.85, 1.7, or 3.4 mol% of Ni (based on Ni surface atoms), and 2 mL of toluene were added. The flask was then introduced in a preheated 130 °C oil-bath for 24 h to evaluate the effect of the catalyst loading (Figure 6b).

***Hot filtration experiments***: The hot filtration test involves the filtration of a part of the catalytic reaction maintaining the reaction conditions and monitoring the reaction time profile in the remaining filtrate. In the dehydrogenation of alcohols, the reaction mixture was filtered off trough celite at 130 °C after 1 h of reaction (GC conversion approx. 40%). The filtrate was maintained under general reaction conditions after the addition of the corresponding amount of base ($Cs_2CO_3$ 0.15 mmol) for 24 h, but no further dehydrogenation was observed (Figure 8); therefore, this indicates that the catalytic active species are heterogeneous.

***Recycling experiments***: After performing a general catalytic experiment, the solid catalyst **NiNPs/NHCs@rGO** was filtered and was washed with toluene (3 ×5 mL), water (3 ×5 mL), and acetone (2 × 5 mL). After drying with acetone, the recovered solid catalyst was then used in another run without employing any regeneration process. Reaction evolution and yield were calculated using the general procedure described in the catalytic experiments. Conditions: 0.15 mmol of benzyl alcohol, 2 equiv. of $Cs_2CO_3$, 1.7 mol% of Ni (surface atoms), and 2 mL of toluene.

## Supporting Information

The authors have cited additional references within the Supporting Information.[74] Additional characterization materials by ESI–MS, XPS, Raman, HRTEM, and single X-ray diffraction.[75] Further details of experimental procedures, NMR characterization of organic products, and details of quantification analysis.

## Acknowledgements

The authors thank the Spanish Ministry of Science and Innovation for financial support through the project PID2021-126071OB-C22 and CEX2023-001286-S, funded by MICIN/AEI/10.13039/501100011033/ FEDER "Una manera de hacer Europa". Generalitat Valenciana (MFA/2022/043) with funding from European Union NextGenerationEU and Universitat Jaume I (UJI-B2022-23 and GACUJIMB/2023/13) are also gratefully acknowledged. I.S thanks the Grant CNS2022-136183 funded by MICIU/AEI/10.13039/501100011033 and by "European Union

NextGenerationEU/PRTR", and the Grant PID2022-143164OA-I00 funded by MICIU/AEI/10.13039/501100011033 and by "ERDF/EU". J. M-V thanks program "Santiago Grisolia" (GrisoliaP2021/114). The authors thank "Servei Central d'Instrumentació Científica (SCIC) de la Universitat Jaume I". S.M. is grateful to Gobierno de Aragón through the grant E31_23R with European Social Funds (Construyendo Europa desde Aragón).

## Conflict of Interests

The authors declare no conflict of interest.

## Data Availability Statement

The data that support the findings of this study are available in the Supporting Information of this article.

**Keywords:** Acceptorless dehydrogenation · Graphene · Hybrid materials · Nickel nanoparticles · Supported catalysts

[1] N.-D. Jaji, H. L. Lee, M. H. Hussin, H. M. Akil, M. R. Zakaria, M. B. H. Othman, *Nanotechnol. Rev.* **2020**, *9*, 1456–1480.
[2] D. Müller, D. I. Groves, M. Santosh, C.-X. Yang, *Geosyst. Geoenviron.* **2025**, *4*, 100310, https://doi.org/10.1016/j.geogeo.2024.100310.
[3] Y. Sawama, K. Morita, S. Asai, M. Kozawa, S. Tadokoro, J. Nakajima, Y. Monguchi, H. Sajiki, *Adv. Synth. Catal.* **2015**, *357*, 1205–1210.
[4] J. R. Ludwig, C. S. Schindler, *Chem.* **2017**, *2*, 313–316.
[5] F. Alonso, P. Riente, M. Yus, *Acc. Chem. Res.* **2011**, *44*, 379–391.
[6] J.-F. Soulé, H. Miyamura, S. Kobayashi, *J. Am. Chem. Soc.* **2013**, *135*, 10602–10605.
[7] S. Genç, B. Arslan, D. Gülcemal, S. Gülcemal, S. Günnaz, *Org. Biomol. Chem.* **2022**, *20*, 9753–9762.
[8] V. Arora, H. Narjinari, A. Kumar, *Organometallics* **2021**, *40*, 2870–2880.
[9] F. Alonso, P. Riente, M. Yus, *Eur. J. Org. Chem.* **2008**, *2008*, 4908–4914.
[10] K. Inamoto, J. Kuroda, K. Hiroya, Y. Noda, M. Watanabe, T. Sakamoto, *Organometallics* **2006**, *25*, 3095–3098.
[11] M. J. Iglesias, A. Prieto, M. C. Nicasio, *Adv. Synth. Catal.* **2010**, *352*, 1949–1954.
[12] M. A. Rodríguez-Cruz, S. Hernández-Ortega, H. Valdés, E. Rufino-Felipe, D. Morales-Morales, *J. Catal.* **2020**, *383*, 193–198.
[13] V. Ritleng, M. Henrion, M. J. Chetcuti, *ACS Catal.* **2016**, *6*, 890–906.
[14] M. D. de los Bernardos, S. Pérez-Rodríguez, A. Gual, C. Claver, C. Godard, *Chem. Commun.* **2017**, *53*, 7894–7897.
[15] M. G. Avello, S. Golling, L. Truong-Phuoc, L. Vidal, T. Romero, V. Papaefthimiou, N. Gruber, M. J. Chetcuti, F. R. Leroux, M. Donnard, V. Ritleng, C. Pham-Huu, C. Michon, *Chem. Commun.* **2023**, *59*, 1537–1540.
[16] Z. Dağalan, S. Behboudikhiavi, M. Turgut, M. Sevim, A. E. Kasapoğlu, B. Nişancı, Ö. Metin, *Inorg. Chem. Front.* **2021**, *8*, 2200–2212.
[17] D. Bouzouita, J. M. Asensio, V. Pfeifer, A. Palazzolo, P. Lecante, G. Pieters, S. Feuillastre, S. Tricard, B. Chaudret, *Nanoscale* **2020**, *12*, 15736–15742.
[18] O. Suárez-Riaño, G. Mencia, S. Tricard, J. Esvan, P.-F. Fazzini, B. Chaudret, E. A. Baquero, *Chem. Commun.* **2023**, *59*, 1062–1065.
[19] L. Postigo, B. Royo, *Adv. Synth. Catal.* **2012**, *354*, 2613–2618.
[20] L. P. Bheeter, M. Hedrion, L. Brelot, C. Darcel, M. J. Chetcuti, J. B. Sortais, V. Ritleng, *Adv. Synth. Catal.* **2012**, *354*, 2619–2624.
[21] D. Mateo, J. Albero, H. García, *Appl. Catal. B Environ.* **2018**, *224*, 563–571.
[22] G. Wu, C. Zhang, S. Li, Z. Han, T. Wang, X. Ma, J. Gong, *ACS Sustainable Chem. Eng.* **2013**, *1*, 1052–1062.
[23] L. Gu, C. Zhang, Y. Guo, J. Gao, Y. Yu, B. Zhang, *ACS Sustainable Chem. Eng.* **2019**, *7*, 3710–3714.
[24] S. Chen, J. Duan, J. Ran, M. Jaroniec, S. Z. Qiao, *Energy Environ. Sci.* **2013**, *6*, 3693.
[25] A. P. Prakasham, P. Ghosh, *Inorganica Chim. Acta* **2015**, *431*, 61–100.
[26] F. e Silva, V. Salim, T. Rodrigues, *Appl. Chem.* **2024**, *4*, 86–106.
[27] L. Lu, S. Zou, B. Fang, *ACS Catal.* **2021**, *11*, 6020–6058.
[28] D. Wang, D. Astruc, *Chem. Soc. Rev.* **2017**, *46*, 816–854.
[29] T. Paul, P. P. Saikia, D. Borah, N. Mahanta, A. Baruah, J. M. Borah, B. J. Saikia, K. Raidongia, R. K. Gogoi, R. Gogoi, *ChemistrySelect* **2023**, *8*, 101195.
[30] A. Charvieux, J. B. Giorgi, N. Duguet, E. Métay, *Green Chem.* **2018**, *20*, 4210–4216.
[31] J. Wang, M. Zhang, T. Miao, Y. Ling, Q. Wen, J. Zheng, J. Xu, T. Hayat, N. S. Alharbi, *Inorg. Chem. Front.* **2018**, *5*, 844–852.
[32] D. Astruc, *Nanoparticles and Catalysis*, Wiley-VCH Verlag GmbH & Co. KGaA, Weinheim, Germany **2007**.
[33] A. Mollar-Cuni, D. Ventura-Espinosa, S. Martín, Á. Mayoral, P. Borja, J. A. Mata, *ACS Omega* **2018**, *3*, 15217–15228.
[34] D. Ventura-Espinosa, S. Martín, H. García, J. A. Mata, *J. Catal.* **2021**, *394*, 113–120.
[35] D. Teichmann, W. Arlt, P. Wasserscheid, *Int. J. Hydrogen Energy* **2012**, *37*, 18118–18132.
[36] P. M. Modisha, C. N. M. Ouma, R. Garidzirai, P. Wasserscheid, D. Bessarabov, *Energy Fuels* **2019**, *33*, 2778–2796.
[37] K. Müller, K. Stark, V. N. Emel'yanenko, M. A. Varfolomeev, D. H. Zaitsau, E. Shoifet, C. Schick, S. P. Verevkin, W. Arlt, *Ind. Eng. Chem. Res.* **2015**, *54*, 7967–7976.
[38] P. J. Bonitatibus, S. Chakraborty, M. D. Doherty, O. Siclovan, W. D. Jones, G. L. Soloveichik, *Proc. Natl. Acad. Sci.* **2015**, *112*, 1687–1692.
[39] M. Yadav, Q. Xu, *Energy Environ. Sci.* **2012**, *5*, 9698–9725.
[40] R. H. Crabtree, *Chem. Rev.* **2017**, *117*, 9228–9246.
[41] R. Tan, Q. Ji, Y. Ling, L. Li, *Chem. Commun.* **2024**, *60*, 8186–8203.
[42] C. Berini, O. H. Winkelmann, J. Otten, D. A. Vicic, O. Navarro, *Chem. A Eur. J.* **2010**, *16*, 6857–6860.
[43] B. Landers, O. Navarro, *Inorganica Chim. Acta* **2012**, *380*, 350–353.
[44] T. Paul, P. P. Saikia, D. Borah, N. Mahanta, A. Baruah, J. M. Borah, B. J. Saikia, K. Raidongia, R. K. Gogoi, R. Gogoi, *ChemistrySelect* **2023**, *8*, e202204713.
[45] C. D. Abernethy, A. H. Cowley, R. A. Jones, *J. Organomet. Chem.* **2000**, *596*, 3–5.
[46] C. D. Abernethy, J. A. C. Clyburne, A. H. Cowley, R. A. Jones, *J. Am. Chem. Soc.* **1999**, *121*, 2329–2330.
[47] R. A. Kelly, N. M. Scott, S. Díez-González, E. D. Stevens, S. P. Nolan, *Organometallics* **2005**, *24*, 3442–3447.
[48] D. Ventura-Espinosa, S. Sabater, J. A. Mata, *J. Catal.* **2017**, *352*, 498–504.
[49] D. Ventura-Espinosa, S. Sabater, A. Carretero-Cerdán, M. Baya, J. A. Mata, *ACS Catal.* **2018**, *8*, 2558–2566.
[50] S. Sabater, J. A. Mata, E. Peris, *ACS Catal.* **2014**, *4*, 2038–2047.
[51] D. Ventura-Espinosa, A. Marzá-Beltrán, J. A. Mata, *Chem. A Eur. J.* **2016**, *22*, 17758–17766.
[52] D. Ventura-Espinosa, C. Vicent, M. Baya, J. A. Mata, *Catal. Sci. Technol.* **2016**, *6*, 8024–8035.
[53] A. Mollar-Cuni, P. Borja, S. Martin, G. Guisado-Barrios, J. A. Mata, *Eur. J. Inorg. Chem.* **2020**, *2020*, 4254–4262.
[54] Z. Ji, X. Shen, G. Zhu, H. Zhou, A. Yuan, *J. Mater. Chem.* **2012**, *22*, 3471–3477.
[55] P. Veerakumar, S.-M. Chen, R. Madhu, V. Veeramani, C.-T. Hung, S.-B. Liu, *ACS Appl. Mater. Interfaces* **2015**, *7*, 24810–24821.
[56] A. Mollar-Cuni, S. Martín, G. Guisado-Barrios, J. A. Mata, *Carbon* **2023**, *206*, 314–324.
[57] A. Al-Nafiey, A. Kumar, M. Kumar, A. Addad, B. Sieber, S. Szunerits, R. Boukherroub, S. L. Jain, *J. Photochem. Photobiol. A Chem.* **2017**, *336*, 198–207.
[58] R. Ye, A. V. Zhukhovitskiy, R. V. Kazantsev, S. C. Fakra, B. B. Wickemeyer, F. D. Toste, G. A. Somorjai, *J. Am. Chem. Soc.* **2018**, *140*, 4144–4149.
[59] J. C. Espinosa, M. Álvaro, A. Dhakshinamoorthy, S. Navalón, H. García, *ACS Sustainable Chem. Eng.* **2019**, *7*, 15948–15956.
[60] L. Enders, D. S. Casadio, S. Aikonen, A. Lenarda, T. Wirtanen, T. Hu, S. Hietala, L. S. Ribeiro, M. F. R. Pereira, J. Helaja, *Catal. Sci. Technol.* **2021**, *11*, 5962–5972.
[61] C. Zhang, K. Zheng, X. Ye, D. Yang, L. Zhou, K. Liang, J. Yun, *Chem. Eng. Sci.* **2025**, *304*, 120980.
[62] X. Pan, Y. Zhu, Y. Yang, Q. Zhu, *Nanomaterials* **2024**, *14*, 744.

[63] Y. Huang, X. Chong, C. Liu, Y. Liang, B. Zhang, *Angew. Chem., Int. Ed.* **2018**, *57*, 13163–13166.
[64] S. Zhu, Y. Chen, X. Gao, Z. Lv, Y. He, J. Wang, W. Fan, *Catal. Sci. Technol.* **2020**, *10*, 2786–2796.
[65] J. Meng, Z. Tong, H. Sun, Y. Liu, S. Zeng, J. Xu, Q. Xia, Q. Pan, S. Dou, H. Yu, *Adv. Sci.* **2022**, *9*, 1–10.
[66] M. S. Mirhosseyni, F. Nemati, *Micropor. Mesopor. Mater.* **2022**, *329*, 111514.
[67] J. Huang, J. Xi, W. Chen, Z. Bai, *Acta Chim. Sin.* **2021**, *79*, 1360.
[68] A. Mollar-Cuni, D. Ventura-Espinosa, S. Martín, H. García, J. A. Mata, *ACS Catal.* **2021**, *11*, 14688–14693.
[69] M. Yang, A. Lenarda, S. Frindy, Y. Sang, V. Oksanen, A. Bolognani, L. Hendrickx, J. Helaja, Y. Li, *Proc. Natl. Acad. Sci.* **2023**, *120*, 2017–2026.
[70] D. Ventura-Espinosa, A. Carretero-Cerdán, M. Baya, H. García, J. A. Mata, *Chem. – A Eur. J.* **2017**, *23*, 10815–10821.
[71] R. Porcar, A. Mollar-Cuni, D. Ventura-Espinosa, S. V. Luis, E. García-Verdugo, J. A. Mata, *Green Chem.* **2022**, *24*, 2036–2043.
[72] D. Ventura-Espinosa, S. Martín, J. A. Mata, *J. Catal.* **2019**, *375*, 419–426.
[73] S. Sabater, J. A. Mata, E. Peris, *Organometallics* **2012**, *31*, 6450–6456.
[74] G. C. Bond, in *Metal-Catalysed Reactions of Hydrocarbons* (Ed: G. C. Bond), Springer, Boston, US **2005**, pp. 35–91.
[75] Deposition Number 2394528 (for 2) Contains the Supplementary Crystallographic Data for This Paper. These Data Are Provided Free of Charge by the Joint Cambridge Crystallographic Data Centre and Fachinformationszentrum Karlsruhe Access Structures Service.

Manuscript received: April 2, 2025
Accepted manuscript online: April 3, 2025
Version of record online: ■■, ■■